Study of defects in directed energy deposited Vanadis 4 Extra tool steel
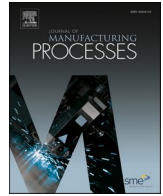
(article starts on next page)

Study of defects in directed energy deposited Vanadis 4 Extra tool steel

Miwen Yuan [a,b], Seshendra Karamchedu [c], Yicheng Fan [d], Libin Liu [a], Lars Nyborg [b], Yu Cao [b,*]

[a] *School of Materials Science and Engineering, Central South University, Changsha 410083, PR China*
[b] *Department of Industrial and Materials Science, Chalmers University of Technology, Gothenburg 41296, Sweden*
[c] *Uddeholms AB, Hagfors 638 85, Sweden*
[d] *ASSAB Tooling Technology (ShangHai) Co., Ltd, Shanghai 201108, PR China*

ABSTRACT

A cold work tool steel with varied number of layers was deposited on a substrate of hot work tool steel for hard-facing by directed energy deposition technique. This study deals with the defects and microstructure in the as-cladded tool steels. Defects, including pores and cracks, were found in the deposited zone, the number of which increased with the building height or number of layers deposited. Large irregular pores were mainly located at the lower regions of the deposited layers. The formation of this type of pores was attributed to the segregation of alloy elements on the pore surface and insufficient heat input. Non-equilibrium eutectic microstructure was a characteristic feature in the regions adjacent to the pores. Cracking, on the other hand, tended to occur in the upper part of the deposited layers. Two important contributing factors were identified for cracking. The first one was the microstructural gradient, which was modified from fine cellular dendrite to columnar dendrite when moving from the bottom to the top deposited layer. Second, the deposited cold work tool steel exhibited a relatively large temperature range of solidification, as simulated by Thermocalc software, leading to high sensitivity to hot cracking.

1. Introduction

In manufacturing within the automotive segment, hot forming of sheet material is an area where high demands are placed on the tooling. The tools for this application are generally produced using hot work H13 steel. In many cases, the tool life and in turn the production cost is determined by the wear of the tools. This is more prominent in the case when un-coated sheet materials are formed. It is thus of great importance to improve the wear resistance of the hot work tool steel. Surface coating can be used for this purpose [1] by increasing surface hardness and reducing the friction between mold and work piece.

In recent years, additive manufacturing (AM) has attracted lots of attention from both industry and academia. In AM, parts are fabricated through layer-by-layer addition of materials. This novel method can produce parts with highly complex shapes [2,3] and functionality gradients [2,4], which are almost impossible to obtain through conventional casting or machining of wrought material. Due to these unique characteristics, it is widely used for metallic, organic and inorganic materials in applications across various industrial domains such as aerospace, automotive, medical implants and tooling. Powder bed fusion (PBF) and directed energy deposition (DED) are two widely

applied AM methods for metallic materials. During DED, which is utilized in this study, the feedstock materials are delivered to the melt pool created by a moving heating-source and melted. Laser beam, electron beam and electric arc are three main heating sources employed for this technique. The properties obtained for materials and components produced through the PBF method are generally superior to those produced by DED. However, in some cases, the components produced through the latter could exhibit relatively superior mechanical properties due to less defects and higher reliability [5]. For example, Xue reported that the as-printed H13 tool steel fabricated by DED method has outstanding tensile strength (2033–2064 MPa) and elongation (5–6%), which is comparable to the wrought material. Additionally, DED method enables fabrication of the components with gradient functionality and microstructures by means of a deposition machine mounted with two or more powder feeders using proper powder feed ratio [4]. In general, subsequent heat treatment is required after DED, to eliminate or minimize the residual stress, which can be otherwise detrimental to the geometrical control and mechanical properties [6].

Tooling is an area where additive manufacturing (AM) is beneficial owing to the low volume series combined with challenges related to design complexity and high-performance requirements. Considering

wear resistance, those tool steels used for cold work applications stand out compared to those used in hot-work applications. Hence, to improve the wear resistance of the molds used for hot forming, Uddeholms Vanadis 4 Extra (V4E), a cold work steel with excellent wear resistance, was deposited on a modified H13 hot work tool steel (Uddeholm Dievar) by DED in the present study. It is expected that DED can be used not only as a means to impart wear resistance to this hot work tool steel, to delay the advent of wear but also as a means of repair.

During the AM process, defects are commonly encountered and challenge the fabrication of metallic materials. Defects, such as lack of fusion, pores and cracks, would have a deleterious impact on the mechanical properties of AM metal parts. For tool steels with high hardness, high strength and poor ductility, cracking is a particularly serious problem during the AM processing, especially for some cold work tool steels. Many studies have been focused on the quality improvement of hot work tool steels, such as H13 steel [7–11]. The studies related to cold work tool steel are limited due to the high cracking susceptibility. Usually, high content of carbon and alloy elements, characteristic of cold work tool steels, implies a low processability [12–14]. For example, detached built-layers have been observed in X65MoCrWV3-2 cold work tool steel parts produced by PBF [12]. Barr et al. [13] studied the cracking sensitivity of Aermat 100 deposited on substrate of 4340 steel and 300M steel. The authors reported that cracks were found in the deposited zone with only 1 layer. This was attributed to unsynchronized solidification which led to insufficient feeding and initiation of cracking. The processability in DED is also affected by oxygen [15] and carbon [16] content in tool steel. Preheating the baseplate has been found to be effective to suppress the formation of cracks [12]. When preheating the built plates to 300 °C, the crack density could decrease from $6.98 \cdot 10^{-4}$ μm^{-1} to $0.41 \cdot 10^{-4}$ μm^{-1} due to reduced thermal stresses. In the context of DED, synergy between the deposition and solidification is critical.

Hot cracking is one of the major challenges in DED. It is generally accepted that it is related to the high thermal tensile stress produced by the volumetric shrinkage caused by uneven cooling between different layers and the thermal shrinkage between the liquid and its adjacent grains [17]. Thermal stress is always associated with the thermal expansion coefficient α. The materials with a high α (like aluminium alloy) usually have high cracking susceptibility. However, solidification and thermal stress conditions are influenced by the periodic heating history in DED, making the cracking phenomena complex to investigate. Nevertheless, pre-heating and optimization of processing parameters still provides an opportunity to build non-weldable materials through DED method, as confirmed in the case of Ni base alloys [18] and high strength steels (HSS) [19–21].

Most of the literatures related to tool steels produced by DED focus on single layer deposition. Cracking problems still plague the multi-layer deposition of tool steels. In the present study, Vanadis 4 Extra with 1, 2 and 4 layers were deposited on a hot work tool steel of modified H13 composition (Uddeholm Dievar) to investigate the influence of build height on defect formation and microstructure evolution. Although preheating the baseplate is a possible way to prohibit cracking, it will add an additional step to the AM process, which increases cost and can also lead to undesirable geometrical changes in the tool. Hence, it would be meaningful to explore the possibility to deposit a cold work tool steel on another tool steel without preheating and to understand the limits of the same. In this context, more in-depth understanding of defects formation in the DED process of advanced tool steel is of great importance.

2. Experiments

Pre-alloyed V4E powders and Dievar steel baseplate were provided by Uddeholms AB, Sweden. The composition of two steels is shown in Table 1. The powder utilized for this study was sieved between 45 and 150 μm with D10, D50 and D90 of 52, 73 and 125 μm respectively. The Hall flow rate was 15 s, and the apparent density of the powder was 4.4 g/cm^3. The substrate material was Dievar and the bulk dimension was

Table 1

The chemical composition of two steels involved in this study comprising the deposited material (V4E) and the substrate material (Dievar) (wt%).

	C	Si	Mn	Cr	Mo	V
V4E	1.4	0.4	0.4	4.7	3.5	3.7
Dievar	0.35	0.2	0.5	5.0	2.3	0.6

$117 \times 59 \times 25$ mm^3. Surface deposition was performed by a 5-axis DED laser machine equipped with a 4000 W laser. The focal distance of co-axial powder feeding nozzles was 16 mm. The shielding gas employed was argon with a flow rate of 18 L/min. The thickness of each layer was 1.6 mm. The deposition parameters are presented in Table 2. Different layers (1, 2 and 4) were deposited on the baseplate which was not preheated before deposition. The deposited samples are illustrated in Fig. 1.

After DED, no macro-cracking or distortion was observed. Cubic specimens with a size of $10 \times 10 \times 10$ mm^3 were extracted from the center part of bulk samples to avoid edge effects. Both YZ and XY plane of samples, as indicated in Fig. 1, were ground and polished following the standard Struers metallographic procedures. Microstructure characterization was performed on cross sections (i.e., the YZ plane) using samples etched with an etchant consisting of 5% picric acid + 1% HCl + 94% ethanol for 30 s. Optical images were recorded by mean of optical microscopy (OM) using Carl Zeiss Axioscope 7 instrument. To survey the defect distribution in the deposited layers, ImageJ software (version v1.52p) was used on stitched OM images (with a magnification of 50 ×). First, the analyzed OM images were binarized. Subsequently, the average porosity was obtained by measuring the area fraction of black pixels in the analyzed images. For all the samples with varied number of layers, 8 stitched overview OM images were used for the assessment of average porosity. Relative density is defined as $(1 - \text{porosity}) \times 100\%$. The microstructure was further observed using a LEO/ZEISS Gemini 1550 Scanning Electron Microscope (SEM). Chemical composition was analyzed by energy-dispersive X-ray spectroscopy (EDX), using an Oxford Dispersive spectrometer equipped on the SEM. In order to investigate the chemistry in the neighborhood of the pores, a bar-shaped specimen extracted from 4-layers sample was broken with a hammer, to expose the internal surface of the voids. A PHI 700 Scanning Auger Electron Spectroscopy (AES) was then applied to analyze the composition. Element distribution as a function of depth was determined by successive AES analyses and argon ion etchings over an area of 2×2 mm^2 with ion beam accelerating voltage of 2 kV. The nominal etch rate was calibrated by using Ta_2O_5/Ta samples with known oxide thickness. To identify the carbides formed, the bulk of the as cladded layer was dissolved using 20% HCl to extract the carbide powder which was then analyzed by means of X-ray diffraction (XRD) using Bruker D8 Advance with a Cu X-ray source (λ = 1.54 Å). The diffraction angle 2θ was between 30° -125° and the step size was 0.02° with 0.4 s per step. By means of Thermo-Calc software (2019a), the phase evolution during the solidification process of V4E was depicted at high cooling rate considering Scheil solidification model using database of Fe-Alloy v9.0. Hardness (Vickers) testing was performed on cross section using a DuraScan 70-G5 machine with a 10 kg load and 10 s dwell time.

Table 2

Experimental parameters used for the deposition of V4E.

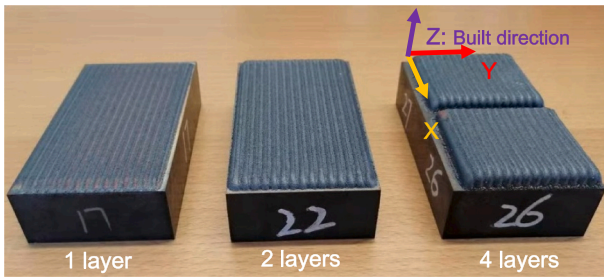|	
Laser power	1.6 kW
Scanning velocity	520 mm/min
Hatch distance	1.8 mm
Powder feeding rate	16 g/mm
Layer thickness	1.6 mm

Fig. 1. As-deposited bulk samples.

3. Results

3.1. Defects and their distribution

Optical microscopic images from cross-sections (YZ plane in Fig. 1) with various deposition layers are presented in Fig. 2. In the images, the laser path direction (X-direction in Fig. 1) of the tracks is perpendicular to the plane of cross-section. The deposition zone (DZ), heat affected zone (HAZ) and substrate could clearly be distinguished in all samples. In the 1-layer sample, no cracks but a few pores were detected, and the corresponding relative density of deposition zone was 99.44 ± 0.45%. In the 2-layer sample, both pores and cracks were observed. The density was estimated to be 99.65 ± 0.33%, which was similar to the 1-layer sample considering the standard deviation. It should be mentioned that the cracks were only observed in the 2nd layer, while the 1st layer was almost crack-free. However, for the 4-layers sample, much more cracks and pores were detected, especially in the 3rd and 4th layers. As expected, the density decreased slightly to 98.73 ± 0.72%. More defects observed in the 3rd and 4th layers indicated the growing tendency of defect formation with increase in building height. Moreover, large pores (≥50 μm) were preferentially located at the interface between layers or at the lower part of the layers. On the contrary, cracking tended to occur in the upper part of the layers. Some long cracks even extended to the next layer. In general, crack propagation was observed along the build direction. It should be pointed out that the first layer was deposited on the hot work base material (Dievar) while the deposition of others took place on the "cold work" (V4E) deposited layer which was expected to be more brittle compared to the hot work base material. This condition was comparable to DED on a cold work tool steel which is challenging due to the generally low weldability of this family of tool steel. Point ①, ② and ③ in Fig. 2c marked with arrows represent typical defects, i.e., pores and cracks, in DZ. The microstructure at these locations will be discussed later.

3.2. General microstructure

For the top layer of DZ, alternating bright and dark areas were observed in the optical images, as exhibited in Fig. 2. Each single track was related to a bright zone and a dark zone (Fig. 3a), which can be explained as follows. When cooling the deposited layer below M_s, martensite was expected to form owing to high hardenability originating from the high concentrations of C and alloying elements in V4E. Some retained austenite was also present. The martensite was tempered and retained austenite was decomposed partly by the heat from the deposition in the next track. Obviously, the region adjacent to the newly formed melt pool had higher tempering temperature. The retained austenite in these regions, i.e., dark regions was expected to be less than that in the bright regions. The consequence was that the areas with less retained austenite were etched more and exhibited darker contrast. The trend in the hardness variation supported this hypothesis, as shown in Fig. 4. Relatively higher hardness in the darker regions of melt pools can be attributed to the reduced retained austenite. Detailed examination of the microstructure in these two zones (marked as Point 1 and Point 2 in Fig. 3a) by means of SEM is presented in Fig. 3b and c. The martensite at point 1 exhibited a needle-type morphology (Fig. 3b). The well-preserved region surrounding the carbides indicated by both solid and dash arrows was suspected to be austenite phase owing to its better corrosion resistance (and hence less affected when being etched). There were mainly two types of carbides observed in the bright zone. The major one was the darkish carbide (marked with solid arrows) distributed at interdendritic regions. Another type of carbide was whitish one marked with dash arrows, this carbide had much lower fraction than the darkish one. For the Point 2 in dark region (Fig. 3c), martensite has coarser morphology compared to that in the point 1 at bright area (Fig. 3b). The matrix was etched more, and the retained austenite only existed in the interdendritic regions at Point 2. Also, the fraction of carbides with brighter contrast seemed to be very small, and these carbides could hardly be detected.

Fig. 5 presents the typical microstructure from the bright areas of different layers. The first layer (Fig. 5a) adjacent to substrate had a cellular structure with darkish and whitish carbides in the shape of short rods along cell boundaries. For the second and third layer, the cellular structure was observed to be coarser, and the darkish carbides became longer. The microstructure of interdendritic regions was no longer pure carbides. Instead, eutectic structure with high fraction of carbides was observed, as indicated in the insert in Fig. 5b and c. In the top layer, columnar dendrite with eutectic structure in the interdendritic region was formed. Regarding the microstructure evolution, heat transfer played a critical role. The heat from the first layer could be transferred
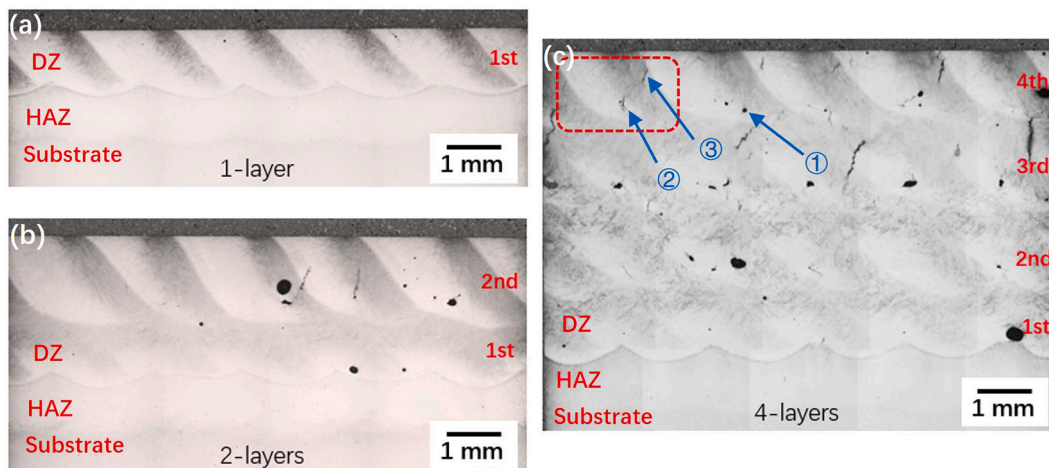

Fig. 2. Cross-sections (YZ plane in Fig. 1) of deposited V4E steel fabricated with (a) 1-layer, (b) 2-layers, (c) 4-layers.
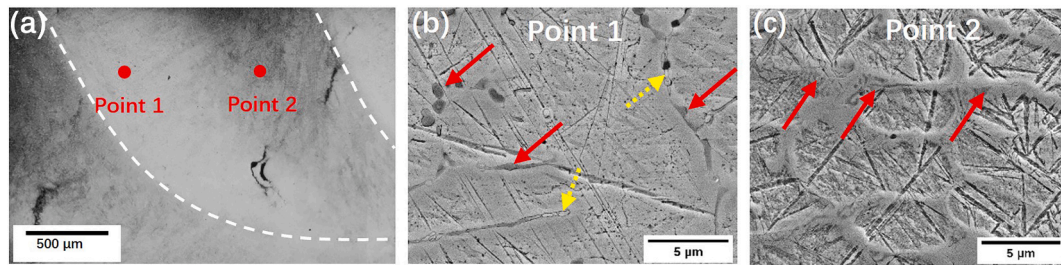
Fig. 3. (a) Top layer zoom-in image from the area in dashed frame of Fig. 2c. (b) and (c) are SEM images of Point 1 and Point 2.
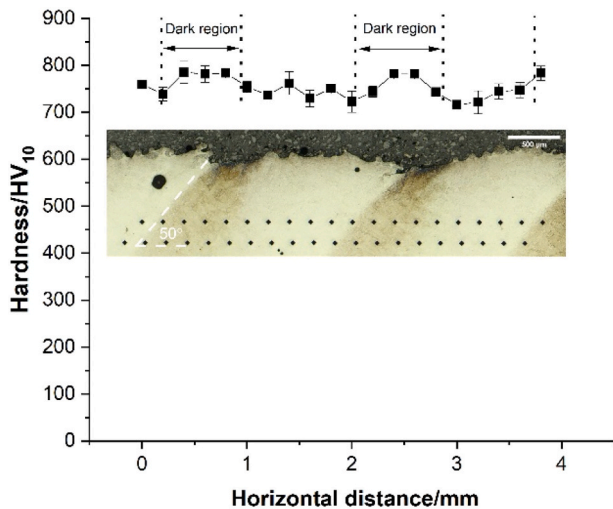

Fig. 4. Hardness profile crossing two melt pools. The second testing row was shift horizontally due to the angle between the melt pool boundary and the horizontal line (50°).

quickly into the substrate which was cold, leading to a fine cellular structure due to its high cooling rate. For the subsequent layers, the peak temperature increased with the build height [28]. Since the new layers were deposited on the previous hot layers, the cooling rate decreased correspondingly. This led to the coarsening of the cellular structure and even the generation of columnar dendrite, as shown in Fig. 5. Moreover, eutectic structure was not observed/obvious (and consequently less defects) for 1-layer sample. Dilution from the substrate could be the explanation. Substrate material (Dievar) had a much lower C and V content compared with V4E. Hence, it was reasonable that the 1st layer (bottom layer) diluted by substrate would have a different solidification path compared to the upper layers and no eutectic structure.

3.3. Carbide identification

Compared to EDX, AES allows inspection of the composition of smaller features due to its higher lateral resolution (in the order of 10 nm). Fig. 6 reveals the typical dendritic structure and the element distribution by AES mapping in as-built V4E steel. In the inter-dendritic regions, two types of carbides were identified as V-rich carbide and Cr- Mo-rich carbides respectively with surrounding austenitic regions. Due to the solute partitioning during the solidification, inter-dendritic regions would have higher content of solute elements. However, formation of carbides consumed C, V, Mo and Cr, which were carbide formers, leading to a lack of these elements in the remaining austenite region. Moreover, inclusions of MnS type were detected in the inter-dendritic region.

In a V4E steel fabricated by electron beam melting (EBM) [29], the V-enriched carbide (darkish) was identified as VC carbide while the Cr-Mo-enriched carbide (whitish) as unstable M_2C and M_6C carbides. In the

present study, the formation of M_6C carbide was not able to be confirmed. Fig. 7 depicts the XRD pattern from extracted carbide powder after dissolving the matrix of the cladded layer by using 20% HCl. Carbides were identified to be of MC and M_2C type. Combining the results from Fig. 6, we can confirm that the darkish carbide is VC carbide, and the whitish carbide is M_2C carbide enriched with Mo and Cr.

3.4. Characteristics of defects and surrounding microstructure

In this section, characterization results of the pores and cracks formed in the deposited 4-layers V4E sample are presented. Fig. 8 presents the solidification microstructure in the regions near the defects ①, ② and ③ in Fig. 2c.

Defect ①, a typical pore, is shown in Fig. 8a. Eutectic structure was found in the area around the pore (Fig. 8a1). This eutectic structure constituted a mixture of carbides and matrix. During solidification, the partitioning of the solutes resulted in uneven distribution of these elements in solid and liquid phases. Gradual enrichment of some solute elements took place in the liquid phase. The eutectic structure was expected to be formed in the last stage of solidification, leading to high fraction of carbides compared to the surrounding matrix. Some small shrinkage pores resulted from insufficient liquid refill were also observed in this region, as shown in Fig. 8a2. Prominent eutectic structure was hence considered as a characteristic feature near pores. The eutectic was also observed surrounding the defect ②, as shown in Fig. 8b2. Considering the eutectic microstructure and the irregular blunt front edge, defect ② was more like a void defect instead of crack.

To investigate the internal surface of the pores, a bar-shape specimen extracted from 4-layers sample was broken with a hammer. Imaging utilizing SEM complemented with EDX mapping were employed to study one irregular large pore on the fracture surface, as shown in Fig. 9. The pore surface was relatively smooth and contained higher amounts of Si and O, as confirmed by EDX analysis on point A in Table 3. Compared to the neighboring regions, higher concentration of oxygen was detected at the internal surface of the pore, which suggested the existence of oxide. In addition, higher Si, Mo and V concentrations were observed by EDX analysis at point A (Table 3).

To identify the oxide formed on the internal surface of this pore, AES depth-profiling was also performed, and the result is presented in Fig. 10. At the top surface of this area, only Si and O were found, indicating the formation of Si oxide layer (zone I). With the increase of depth, the concentration of Si and O declined synchronously. The thickness of Si oxide was estimated to be about 20 nm, below which the concentration of Fe was increased significantly. Meanwhile, enrichment of C and V was observed, and the profile of V followed the one of C, indicating the existence of vanadium carbide VC in this layer. In addition, Mo content was higher than the nominal composition, implying the coexistence of the second type of carbide, i.e., M_2C enriched in Mo and Cr. The thickness of this zone II below the Si oxide layer was about 140 nm. In fact, this zone was consistent with the observation of eutectic structure with a large fraction of carbides adjacent to the pores, as illustrated in Fig. 8a. Beyond a depth of ~160 nm, simultaneously reduced C and V content implied that VC was removed. The remained C
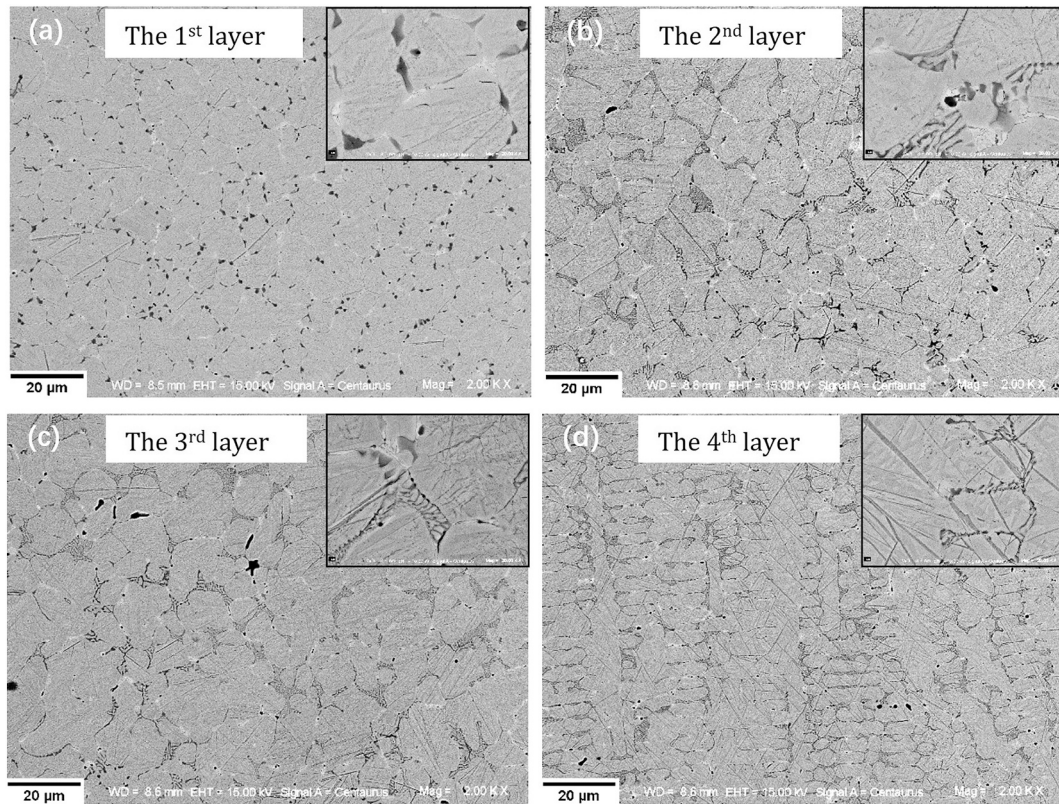
Fig. 5. Comparison of the microstructure from different deposited layers: (a) the 1st layer adjacent to substrate, (b) the 2nd layer, (c) the 3rd layer, (d) the 4th layer (top).
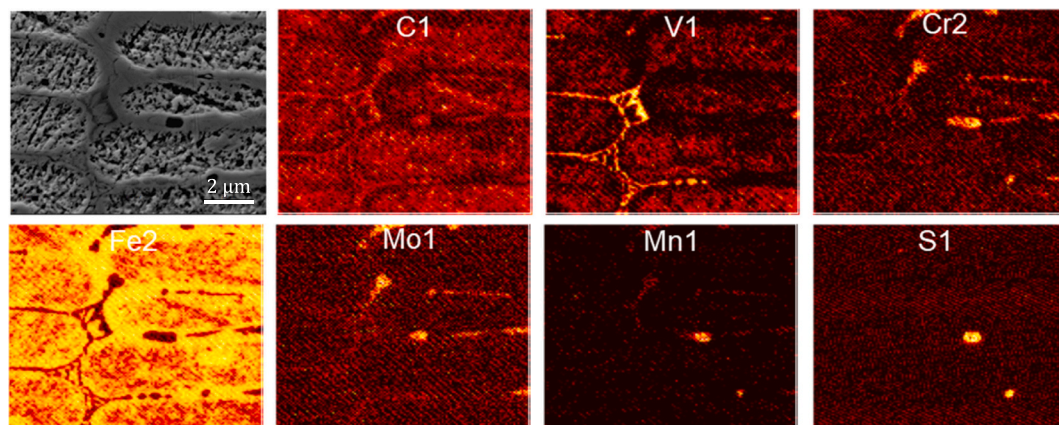

Fig. 6. SEM image and corresponding AES maps of main elements of a typical dendrite region. Dark precipitate enriches in C and V while bright precipitate enriches in Cr, Mo and C.

content and more or less maintained Mo level suggested this region consisted of M_2C together with matrix dominant in Fe (zone III). The eutectic structure will be discussed further in Section 4.2.2.

However, it should be mentioned that not all pores are covered by this Si oxide layer. Oxygen was not detected by EDX at shrinkage pores and spherical pores with a small size. The latter ones probably were keyhole pores formed from the instability at the keyhole tip, which will be discussed in Section 4.1. In summary, there are three types of pores observed in deposited V4E: the macro (larger than 50 μm) pores with silicon oxide layer at the internal surface, spherical keyholes and shrinkage pores. These defects would probably lead to stress concentration when subjected to internal or external stress and acted as initiation points for failures.

In Fig. 8c, c1 and c2, cracks that propagated along the boundaries in dendritic structure are illustrated. More specifically, the interface between carbides and matrix was separated because of the high interfacial energy and the strain energy caused by the carbide formation in most cases. Similar propagation for other cracks was also observed. It was seen from Fig. 2c that most of the cracks were distributed in the upper region of each layer. More cracks observed in the 3rd and 4th layer indicated higher cracking susceptibility with increased build height. Although some cracks were detected at the lower regions of the layers, they were hypothesized to be initiated from pores. The growth of such cracks was probably restricted, as indicated by their limited length and width. The growth of internal cracks would depend on the subsequent conditions, such as the change in thermal stress.
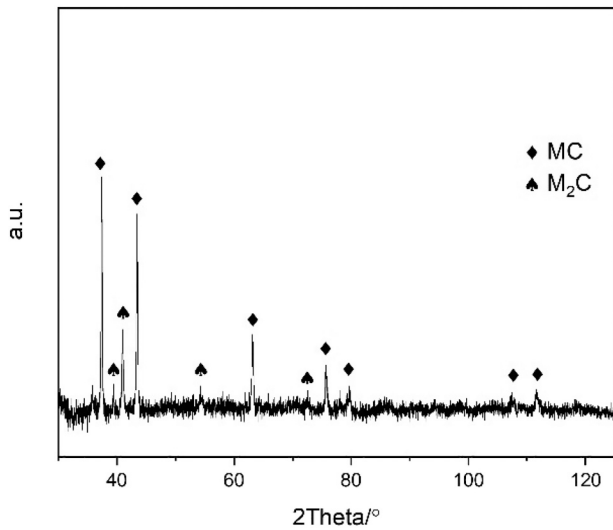
Fig. 7. XRD pattern from carbide powder extracted from the as cladded V4E steel bulk sample.

4. Discussion

4.1. Mechanism of pore formation

The distribution of pores in deposited V4E steel can be clearly seen in Fig. 2. Most of the visible pores are located at the lower region of each layer. As stated in section of 3.4, there are three type of pores: large irregular, shrinkage and keyhole pores. Regarding the formation of keyholes, Zhao [22] investigated the formation mechanism in laser beam powder bed fusion (LB-PBF) by means of Megahertz X-ray technique. It is suggested that the deep and narrow keyhole is generated in the melt pool when the strong recoil pressure from the rapid evaporation of the metal pushes the surrounding molten liquid downwards. Under the complex combination of forces including thermocapillary force, Marangoni flow and the recoil pressure, pores are generated from the instable tip of key holes which is located at the lower position of melt pool. If the cooling rate is fast enough, these pores will be trapped by the solid phase. The original keyhole is not a defect. Only the part left behind and trapped in solid is a defect.

The mechanism for the irregular large pores is different. First, as shown in Figs. 9 and 10, the Si oxide layer is formed at the internal surface of the irregular large pores. It means that the Si in V4E steel is oxidized preferentially and gathered in oxide form at the internal void surfaces during the melting. Such oxide layer may change the surface energy of melt pool and consequently the flow behavior of the melt, preventing the elimination of the pores [23]. Second, Wright et al. [16] reported that the carbon content will largely influence the melt pool wettability. The authors believe that the high carbon content of the layer under the Si oxide layer would increase the stability of pores as well. Third, most of these large pores are located at the bottom of each layer, as shown in Fig. 2. It is reasonable to infer that the formation of these pores is also related to the short duration of liquid at the near boundary region between different tracks. The liquid there has a lower temperature compared to the central portion and will solidify first. Generally, the voids in melt pool are supposed to float up towards the liquid surface of newly deposited layer. However, if the void is near the melt pool boundary, or the heat input is insufficient, the time is not enough for the voids to float up towards the melt pool surface and the voids can therefore be trapped at the bottom of melt pool. Moreover, the liquid at
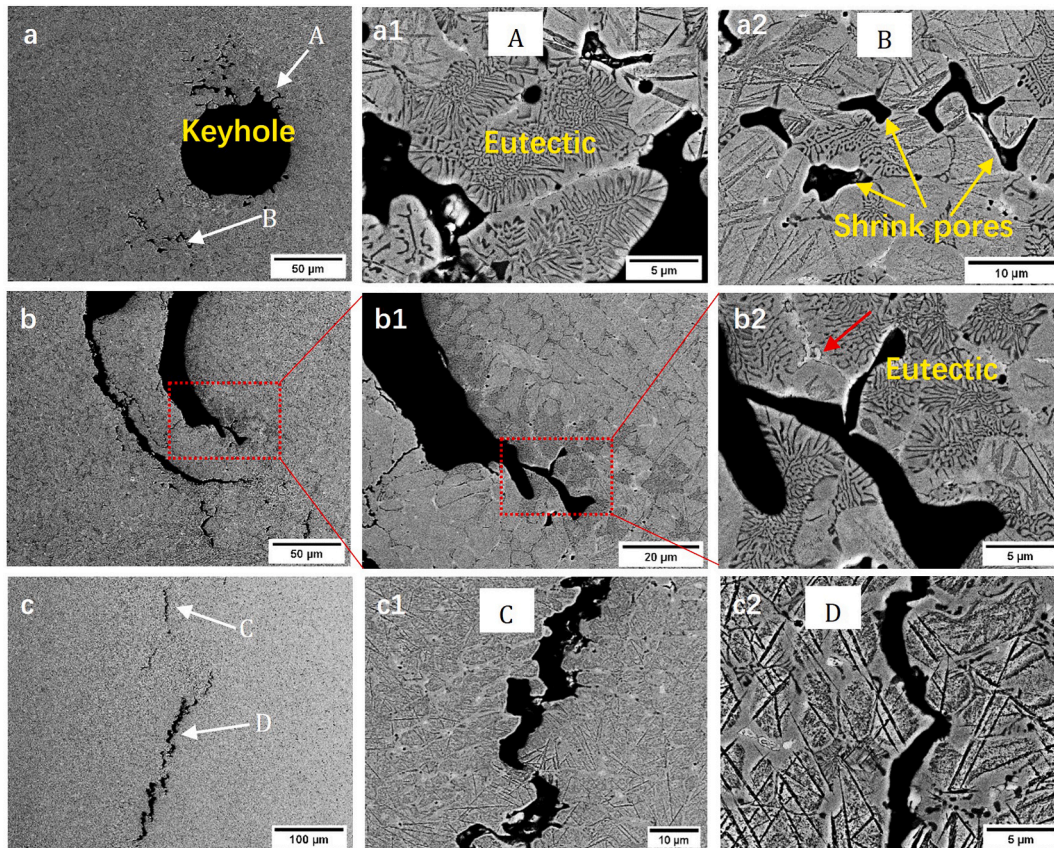

Fig. 8. The SEM images from (a) the pore-type defect ①. (b) The pore-type defect ②, arrow in image b2 shows the bright carbides and (c) the discontinued-cracks ③. Location of defect ①, ② and ③ refer to Fig. 2c.
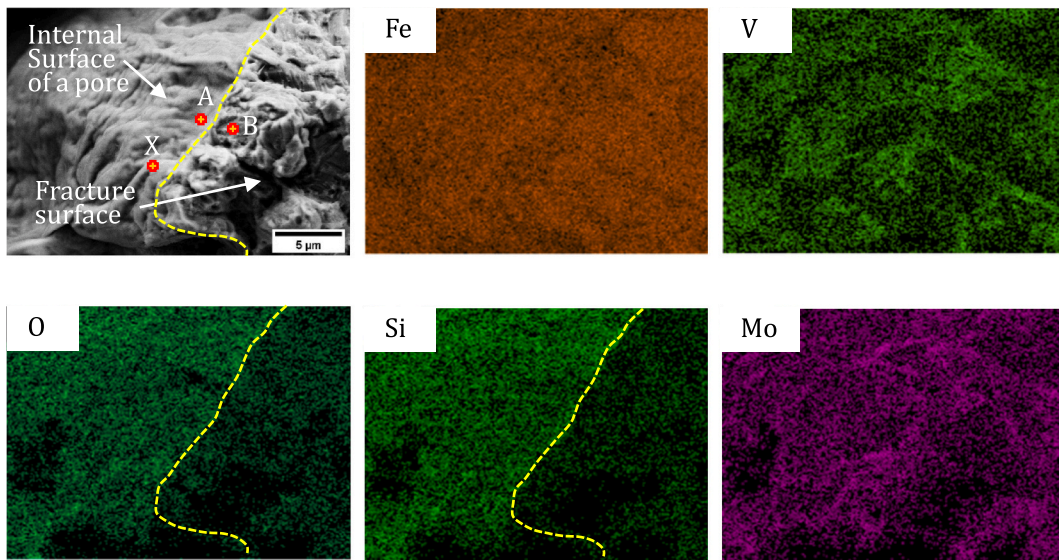
Fig. 9. SEM image and associated EDX maps of the main alloying elements of a region located at the boundary of a void.

Table 3
Chemical composition (wt%) of point A and B located at internal surface of a large pore and neighbor fracture surface as measured by EDX.

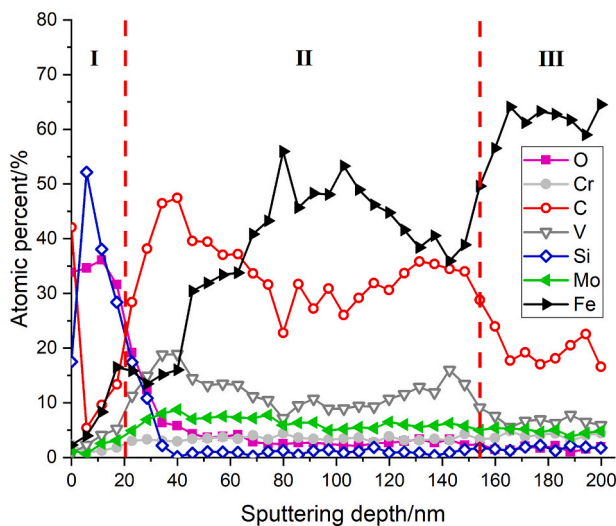| Position	C	O	Si	Mo	Cr	V	Other elements
A	10.8	5.7	2.5	6.9	5.5	4.1	Bal.
B	5.6	–	0.3	2.1	4.1	2.2	Bal.

Fig. 10. AES depth-profiles from point X on the internal surface of the pore in Fig. 9. I: Si oxide, II: containing MC and M_2C carbide, III: containing M_2C carbide.

the near boundary region has a relatively higher viscosity owing to the relative low temperature, which would also inhibit the upward movement/floating of the voids. Hence, the mechanism for the large irregular pores could be attributed to a combination of formation of Si oxide layer and insufficient heat input. For the shrinkage pores, it is generally believed that their formation is caused by the insufficient liquid refill during the solidification.

4.2. Mechanism of crack formation

4.2.1. Stress for cracking

Cracking associated with solidification occurs at the weak locations such as pores or liquid film with stress acting as the trigger. In most cases, this "trigger stress" is thermal stress, which will be discussed below.

In a DED process, the temperature of the newly deposited layer is much higher than the surrounding base materials or previous layers. Such large temperature gradient can induce thermal stress (σ), which is determined by temperature difference (ΔT) of the solid material, elasticity modulus (E) and thermal expansion coefficient (α), as given in Eq. (1) [25]:

$$\sigma = E\alpha(T_f - T_o) = E\alpha\Delta T \tag{1}$$

where T_f, and T_o represent final and initial temperature of the solid respectively. For a given material, the thermal expansion coefficient α and elastic modulus E can be assumed to be constant, even if α is a temperature-dependent property. Thermal stress σ is then mainly determined by the temperature difference. When a newly deposited layer solidifies on the substrate, a tensile stress will be induced in the newly deposited layer. As this tensile stress is proportional to the temperature difference ΔT, increasing the temperature of substrate can reduce ΔT and thereby reduce the thermal stress. Therefore, preheating substrate is a promising means to prohibit hot cracking.

It has been reported [24] that the maximum tensile stress will increase with the build height and prevail in the top layers, which may initiate cracking at the weaker regions. As shown in Fig. 2, significantly less cracks are found in the 1st or 2nd layers, which agrees with this assumption. In addition, the cracks in 1st or 2nd layer are shorter and narrower, which is supposed to be a result of insufficient tensile stress for further propagation. The increased residual tensile stress with building height was also confirmed by the study from Sun et al. [27]. High thermal stress could hence lead to a high cracking susceptibility in the upper layers.

4.2.2. Liquid film

Based on the experimental results discussed previously, a schematic diagram of the solidification process for V4E is presented in Fig. 11. The first solid phase formed from liquid is the cellular/dendritic austenite phase (γ). As the solidification progresses and temperature decreases, non-equilibrium eutectic microstructure is formed consisting of mixture
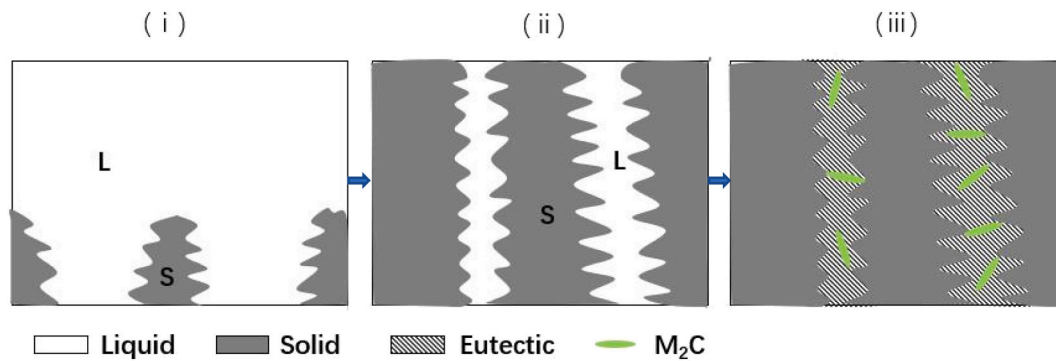
Fig. 11. Schematic illustration of solidification for V4E steel.

of γ and VC carbide (darkish carbides). In the final stage of the solidification, M$_2$C carbide (whitish carbides) is formed from the remaining liquid phase (Fig. 11iii). Thus, the interdendritic region should be the transformation product of the liquid film.

It is known that the compositional segregation has a strong influence on the duration of liquid film through modification of the solidification temperature. Thermo Calc Software (TC) is a suitable tool to evaluate the influence of segregation on solidification. The solidification process of V4E steel was simulated by TC using database of FE9 under the conditions of equilibrium and non-equilibrium (fast cooling rate, Scheil solidification model). The simulated result reveals that the temperature range of non-equilibrium solidification (234 °C) is significantly larger than that of equilibrium condition (142 °C). The larger temperature range suggests that the liquid phase will be maintained at a relative lower temperature during the solidification process than that expected from equilibrium. As can be seen from the Eq. (1), this will contribute to an increase ΔT and consequently higher thermal stress in solid. The liquid phase in interdendritic region will then be vulnerable when the solid experiences thermal contraction, leading to hot cracking. In this cracking mechanism, liquid film is a key factor. Typically, liquid film is referred to as the liquid phase when the percent of solid phase is more than 95%. During the solidification of this liquid film, the wider the temperature range, the higher the cracking susceptibility [30,31]. Since the liquid can be preserved at lower temperatures in non-equilibrium solidification, the melt prevailing over large temperature range results in long channels for backfilling the interdendritic liquid. This makes cracking easier. Oppositely, the melt prevailing over small solidification range results in short channels for backfilling and consequently smaller crack susceptibility. Therefore, rapid cooling at nonequilibrium conditions increases the crack susceptibility dramatically. Moreover, for interdendritic regions with low melting point, re-melting occurs likely when new layer is deposited, leading to the formation of liquid film and accompanied cracking tendency. This is confirmed by the cracks that propagate across the layer boundary in Fig. 2c. To sum up, Scheil simulation can be applied to estimate the temperature range of solidification at nonequilibrium conditions, especially for the last stage of solidification. The result supports the existence of liquid phase film with a low melting point, which will increase the crack susceptibility.

4.2.3. Influence of microstructure on crack susceptibility

As presented in Section 3.2, the bottom layer exhibits a cellular structure, while the top layer has a columnar dendrite structure. This change in microstructure could alter the hot cracking susceptibility. Fine cellular structure has a short backfill channel during the final stage of solidification (solid fraction > 0.8 [26]). Liquid can be supplied easily into the cavity caused by the volumetric solidification shrinkage and thermal contraction. In contrast, the columnar dendrite has a long channel for liquid supplement. This channel can be easily closed by the growth of columnar dendrite. The trapped liquid in the interdendritic region could then form a cavity, which could lead to cracking. In the present study, compared to fine cellular structure, coarser structure and columnar dendrite structure exhibit higher cracking susceptibility. This is an important reason for cracking in upper deposited layers during solidification.

In accordance with the discussion above, a comprehensive summary of cracking is given as follows. At the last stage of solidification (once the backfill channel is closed), the temperature of the liquid film continues to drop until it is completely solidified. Both the cavity and thermal stress can be formed in this area caused by the shrinkage of liquid transformation, leading to the initiation of the cracks. Subsequent cooling of the solidified materials will intensify the thermal stress, which promotes the crack growth along the interdendritic regions due to the weak bonding between matrix and carbides. Hot crack susceptibility has a close relationship with solidification condition (such as cooling rate, preheating etc.), material characteristics (for instance, thermal expansion coefficient, elastic modulus, thickness of deposited layers etc.) and stress distribution as well as microstructure.

5. Summary and conclusions

Uddeholm Vanadis 4 Extra (V4E) cold work tool steel was deposited on Dievar hot work tool steel with varying number of layers by DED. The major conclusions from present work are summarized as follows.

1. Defects are found in the deposited zone in all the samples. However, 1-layer and 2-layers samples exhibit a higher relative density (>99.4%) with less defects. The 4-layers sample shows significantly more porosity and hot cracking defects in the deposited zone. Large pores (≥50 μm) are preferentially located at the interface between layers or at the lower part of the layers. On the contrary, cracks tend to occur in the upper part of the layers (typically 3rd and 4th layer).

2. There are three types of pores in the deposited zone: the large irregular pores, keyhole pores and shrinkage pores. Thin Si oxide layer was found at the surface of the internal large irregular pores, below which carbides were detected. The formation of this type of pores is attributed to a combination of formation of Si oxide layer, and insufficient heat input.

3. The hot cracking observed in the deposited zone is related to several factors, including intrinsic characteristics of V4E (e.g., wide temperature range of solidification, low plasticity), building height and the microstructure which changes from cellular to columnar dendrite with the increase in building height.

4. Each cladded track is characterized by a bright zone and a dark zone on the optical micrographs. The dark zone is affected more by the next track and contains less retained austenite than that in the bright regions. In addition, martensite is slightly thicker in morphology in this region. There are mainly two types of carbides and the major one distributed in the interdendritic regions is V-rich carbide in the form of MC. Another type of carbide with much lower fraction is identified as Mo- Cr-rich carbide in the form of M$_2$C.

5. A solidification model for V4E in interdendritic region is proposed. Non-equilibrium eutectic microstructure consisting of a mixture of γ and MC carbide is considered as a characteristic feature in the region adjacent to the pores. In the final stage of the solidification, M_2C carbide (whitish carbides) is formed from the remaining liquid phase following eutectic reaction.

Declaration of competing interest

The authors declare that they have no known competing financial interests or personal relationships that could have appeared to influence the work reported in this paper.

References

[1] Berns H, Fischer A. Microstructure of Fe-Cr-C hardfacing alloys with additions of Nb, Ti and B. Mater Charact 1997;39:499–527.
[2] du Plessis A, et al. Beautiful and functional: a review of biomimetic design in additive manufacturing. Addit Manuf 2019;27:408–27.
[3] Sing SL, An J, Yeong WY, Wiria FE. Laser and electron-beam powder-bed additive manufacturing of metallic implants: a review on processes, materials and designs. J Orthop Res 2016;34:369–85.
[4] Carroll BE, et al. Functionally graded material of 304L stainless steel and inconel 625 fabricated by directed energy deposition: characterization and thermodynamic modeling. Acta Mater 2016;108:46–54.
[5] Khodabakhshi F, Gerlich AP. Potentials and strategies of solid-state additive friction-stir manufacturing technology: a critical review. J Manuf Process 2018;36:77–92.
[6] Deirmina F, Peghini N, Almangour B, Grzesiak D, Pellizzari M. Heat treatment and properties of a hot work tool steel fabricated by additive manufacturing. Mater Sci Eng A 2019;753:109–21.
[7] Surshuwlhv P, Wrro RI, Sduwv V, Lqgv DERD, Xpehhfn DUD. Influence of powder bed preheating on microstructure and mechanical properties of H13 tool steel SlM parts. Phys Procedia 2016;83:882–90.
[8] Telasang G, Dutta Majumdar J, Padmanabham G, Tak M, Manna I. Effect of laser parameters on microstructure and hardness of laser clad and tempered AISI H13 tool steel. Surf Coat Technol 2014;258:1108–18.
[9] Kattire P, Paul S, Singh R, Yan W. Experimental characterization of laser cladding of CPM 9V on H13 tool steel for die repair applications. J Manuf Process 2015;20:492–9.
[10] R GP, Kamaraj M, Bakshi SR. Hardfacing of AISI H13 tool steel with Stellite 21 alloy using cold metal transfer welding process. Surf. Coatings Technol. 2017;326:63–71.
[11] Bailey NS, Katinas C, Shin YC. Laser direct deposition of AISI H13 tool steel powder with numerical modeling of solid phase transformation, hardness, and residual stresses. J Mater Process Technol 2017;247:223–33.
[12] Boes J, Röttger A, Mutke C, Escher C, Theisen W. Microstructure and mechanical properties of X65MoCrWV3-2 cold-work tool steel produced by selective laser melting. Addit Manuf 2018;23:170–80.
[13] Barr C, Da Sun S, Easton M, Orchowski N, Matthews N, Brandt M. Influence of macrosegregation on solidification cracking in laser clad ultra-high strength steels. Surf Coat Technol 2017;340(8):126–36.
[14] Liu Z, Qi H. Effects of substrate crystallographic orientations on crystal growth and microstructure formation in laser powder deposition of nickel-based superalloy. Acta Mater 2015;87:248–58.
[15] Das S. Physical aspects of process control in selective laser sintering of metals. Adv Eng Mater 2003;5:701–11.
[16] Wright CS, Youseffi M, Akhtar SP, Childs THC, Hauser C, Fox P. Selective laser melting of prealloyed high alloy steel powder beds. Mater Sci Forum 2006;514–516:516–23.
[17] Eskin DG, Suyitno JF, Mooney L. Katgerman, contraction of aluminum alloys during and after solidification. Metall Mater Trans A 2004;35A:1325–35.
[18] Segerstark A, Andersson J, Svensson LE. Investigation of laser metal deposited alloy 718 onto an EN 1.4401 stainless steel substrate. Opt Laser Technol 2017;97:144–53.
[19] Park JS, Park JH, Lee MG, Sung JH, Cha KJ, Kim DH. Effect of energy input on the characteristic of AISI H13 and D2 tool steels deposited by a directed energy deposition process. Metall Mater Trans A Phys Metall Mater Sci 2016;47:2529–35.
[20] Sun G, Bhattacharya S, Dinda GP, Dasgupta A, Mazumder J. Microstructure evolution during laser-aided direct metal deposition of alloy tool steel. Scr Mater 2011;64:454–7.
[21] Kürnsteiner P, Wilms MB, Weisheit A, Barriobero-Vila P, Jägle EA, Raabe D. Massive nanoprecipitation in an Fe-19Ni-xAl maraging steel triggered by the intrinsic heat treatment during laser metal deposition. Acta Mater 2017;129:52–60.
[22] Zhao C, Parab ND, Li X, Fezzaa K, Tan W, Rollett AD, Sun T. Critical instability at moving keyhole tip generates porosity in laser melting. Science 2020;370:1080–6.
[23] Louvis E, Fox P, Sutcliffe CJ. Selective laser melting of aluminium components. J Mater Process Technol 2011;211:275–84.
[24] Mercelis P, Kruth JP. Residual stresses in selective laser sintering and selective laser melting. Rapid Prototyp J 2006;12(5):254–65.
[25] Callister WD, Rethwisch DG. Materials Science and Engineering: An Introduction9. New York: Wiley; 2018.
[26] Eskin DG, Suyitno, Katgerman L. Mechanical properties in the semi-solid state and hot tearing of aluminium alloys. Prog. Mater. Sci. 2004;49:629–711.
[27] Sun G, Zhou R, Lu J, Mazumder J. Evaluation of defect density, microstructure, residual stress, elastic modulus, hardness and strength of laser-deposited AISI 4340 steel. Acta Mater 2015;84:172–89.
[28] Manvatkar V, De A, Debroy T. Heat transfer and material flow during laser assisted multi-layer additive manufacturing. J Appl Phys 2014;116:124905.
[29] Botero C, et al. Additive manufacturing of a cold-work tool steel using electron beam melting. Steel Res Int 2020;91:2–7.
[30] Zhang J, Singer RF. Hot tearing of nickel-based superalloys during directional solidification. Acta Mater 2002;50:1869–79.
[31] Rappaz M, Drezet JM, Gremaud M. A new hot-tearing criterion. Metall. Mater. Trans. A Phys. Metall. Mater. Sci. 1999;30:449–55.